INL/EXT-20-59174

Three-Phase Modeling in Sockeye

July 2020

J.E. Hansel
R.A. Berry

Changing the World's Energy Future

INL is a U.S. Department of Energy National Laboratory operated by Battelle Energy Alliance, LLC

INL/EXT-20-59174

Three-Phase Modeling in Sockeye

J.E. Hansel
R.A. Berry

July 2020

Idaho National Laboratory
Modeling and Simulation Department
Idaho Falls, Idaho 83415

http://www.inl.gov

Prepared for the
U.S. Department of Energy
Office of Nuclear Energy
Under DOE Idaho Operations Office
Contract DE-AC07-05ID14517

Page intentionally left blank

ABSTRACT

The heat pipe simulation tool, Sockeye, has been given the capability to allow for the presence of the solid phase of the heat pipe working fluid, which is necessary for modeling transients to and from room temperature, since microreactor designs feature high-temperature heat pipes employing metal working fluids. The liquid phase equations have been converted to equations for the mixture of liquid and solid phases, with a simple latent heat relation determining the fractions of these phases. This capability is introduced while preserving equivalent solutions for the liquid-vapor regime. Theory is also presented, as well as numerical examples to illustrate the propagation of a melt front and startup from the solid state.

Page intentionally left blank

CONTENTS

FIGURES

TABLES

Page intentionally left blank

ACRONYMS

HPTAM	Heat Pipe Transient Analysis Model
THROHPUT	Thermal Hydraulic Response of Heat Pipes Under Transients
PDE	partial differential equation

Page intentionally left blank

Three-Phase Modeling in Sockeye

1. INTRODUCTION

Many microreactor designs employ heat pipes as the primary heat transport mechanism. Due to high temperatures at which these reactors are to be operated, these heat pipes use liquid metals, such as sodium or potassium, as the working fluid. While normal operation occurs with the working fluid fully melted, startup and shutdown of the reactor involves temperatures at which the working fluid is partially or completely solid. For multi-physics simulations that begin below the melting point, the working fluid simulation must at least account for the heat required to melt the working fluid and bring it up to a temperature at which normal operation can begin, even by skipping over the details of startup. However, these details of startup and shutdown are important if one is interested in an accurate thermal transient, or if one is not assured of successful heat pipe startup, since incorrect heat pipe startup could dry out the heat pipe during the thaw process and lead to a phenomenon known as the frozen startup limit [1], thereby making it ineffective as a heat removal device for the remainder of the transient.

The physics involved in the startup and shutdown processes in a heat pipe are complex. High-temperature heat pipes feature metals, such as sodium and potassium, as the working fluid, which are solid at room temperature. The triple-point pressures of these metals are on the order of 10^{-5} Pa and 10^{-4} Pa, respectively, which is effectively a vacuum. Under these conditions, the vapor is in the free molecular regime rather than in the continuum regime, rendering traditional flow modeling approaches inappropriate. As the vapor heats up, it transitions to continuum flow in the evaporator, and this front gradually makes its way to the condenser end [1]. During the startup process, interactions take place between all three phases of matter of the working fluid, as well as with the wick structure.

A few efforts have been made to simulate the startup process from a frozen state. Hall and Doster developed THROHPUT (Thermal Hydraulic Response of Heat Pipes Under Transients), a 1-D code capable of simulating the melt front in a lithium heat pipe [2]. Tournier and El-Genk developed HPTAM (Heat Pipe Transient Analysis Model), a 2-D code coupling the core, wick/annulus, and wall regions [3] by appropriate interface conditions. Cao and Faghri [4] modeled startup in 2-D by coupling a self-diffusion model for rarefied gas to the compressible Navier-Stokes equations for continuum vapor flow.

Section 0 presents the theory of the melting model incorporated into Sockeye, Section 0 presents some numerical demonstrations of this new capability, and Section 0 provides conclusions.

2. THEORY

The three-phase model modifies the two-phase model discussed previously [5,6,7]; thus, this report will assume an understanding of the two-phase model and only discuss modifications made for the three-phase model.

First, the volume fraction partitioning is modified to include the solid phase (denoted by subscript *s*) and the wick (denoted by subscript *w*):

$$\alpha_v + \alpha_\ell + \alpha_s + \alpha_w = 1. \tag{1}$$

While the inclusion of the wick volume fraction is arguably independent of three-phase modeling, this change is important in melt dynamics because the heat capacity of the wick itself will ultimately affect the amount of heat required to thaw the working fluid. As a result of the inclusion of the wick volume fraction, the cross-sectional area A now includes the wick area:

$$A = \frac{\pi}{4} D_{\text{clad,i}}^2. \tag{2}$$

Then the wick volume fraction is computed as:

$$\alpha_w = \frac{(1-\epsilon)A_{\text{wick}}}{A}, \tag{3}$$

where:

$$A_{\text{wick}} = \frac{\pi}{4}(D_{\text{wick,o}}^2 - D_{\text{wick,i}}^2), \tag{4}$$

and the subscripts "i" and "o" denote "inner" and "outer," respectively.

The three-phase partial differential equations (PDEs) replace the PDEs for liquid volume fraction, mass, and energy with the PDEs corresponding to the liquid-solid-wick mixture, as denoted by the subscript ℓsw:

$$\frac{\partial \alpha_{\ell sw} A}{\partial t} + u_{\text{int}} \frac{\partial \alpha_\ell}{\partial x} A = \mu \left(p_\ell + \Delta p_{\text{cap}} - p_v\right) A - \frac{\Gamma_{\ell \to v}^{\text{int}} \alpha_{\text{int}} A}{\rho_{\text{int}}}, \tag{5}$$

$$\frac{\partial (\alpha\rho)_{\ell sw} A}{\partial t} + \frac{\partial \alpha_\ell \rho_\ell u_\ell A}{\partial x} = -\Gamma_{\ell \to v}^{\text{int}} \alpha_{\text{int}} A, \tag{6}$$

$$\frac{\partial \alpha_\ell \rho_\ell u_\ell A}{\partial t} + \frac{\partial \alpha_\ell (\rho_\ell u_\ell^2 + p_\ell) A}{\partial x} = p_{\text{int}} \frac{\partial \alpha_\ell}{\partial x} A - F_\ell^{\text{wall}} A - \frac{\mu_\ell u_\ell}{K} A_{\text{wick},\ell} + \alpha_\ell \rho_\ell g_x A - \Gamma_{\ell \to v}^{\text{int}} u_{\text{int}} \alpha_{\text{int}} A, \tag{7}$$

$$\begin{aligned} \frac{\partial (\alpha\rho E)_{\ell sw} A}{\partial t} + \frac{\partial \alpha_\ell u_\ell (\rho_\ell E_\ell + p_\ell) A}{\partial x} &= p_{\text{int}} u_{\text{int}} \frac{\partial \alpha_\ell}{\partial x} A + \frac{\partial}{\partial x}\left((\alpha_\ell k_\ell + \alpha_w k_w + \alpha_s k_s) A \frac{\partial T_{\ell sw}}{\partial x}\right) - \\ \bar{p}_{\text{int}} \mu \left(p_\ell + \Delta p_{\text{cap}} - p_v\right) A - F_\ell^{\text{wall}} u_\ell A + \alpha_\ell \rho_\ell g_x u_\ell A + q_{\ell sw}^{\text{wall}} P_{\text{wall}} + q_\ell^{\text{int}} \alpha_{\text{int}} A - \Gamma_{\ell \to v}^{\text{int}} E_\ell^{\text{int}} \alpha_{\text{int}} A, \end{aligned} \tag{8}$$

$$\frac{\partial \alpha_v \rho_v A}{\partial t} + \frac{\partial \alpha_v \rho_v u_v A}{\partial x} = \Gamma_{\ell \to v}^{\text{int}} \alpha_{\text{int}} A, \tag{9}$$

$$\frac{\partial \alpha_v \rho_v u_v A}{\partial t} + \frac{\partial \alpha_v (\rho_v u_v^2 + p_v) A}{\partial x} = p_{\text{int}} \frac{\partial \alpha_v}{\partial x} A - F_v^{\text{wall}} A + \alpha_v \rho_v g_x A + \Gamma_{\ell \to v}^{\text{int}} u_{\text{int}} \alpha_{\text{int}} A, \tag{10}$$

$$\begin{aligned} \frac{\partial \alpha_v \rho_v E_v A}{\partial t} + \frac{\partial \alpha_v u_v (\rho_v E_v + p_v) A}{\partial x} &= p_{\text{int}} u_{\text{int}} \frac{\partial \alpha_v}{\partial x} A + \bar{p}_{\text{int}} \mu \left(p_\ell + \Delta p_{\text{cap}} - p_v\right) A - F_v^{\text{wall}} u_v A + \\ \alpha_v \rho_v g_x u_v A + q_v^{\text{wall}} P_{\text{wall}} + q_v^{\text{int}} \alpha_{\text{int}} A - \Gamma_{\ell \to v}^{\text{int}} E_v^{\text{int}} \alpha_{\text{int}} A. \end{aligned} \tag{11}$$

Pressure relaxation and interfacial heat and mass transfer are disabled until melting begins ($\alpha_\ell > 0$) at a given location, due to the lack of interfacial area between liquid and vapor.

Section 2.1 gives the relations for new quantities appearing in these equations and describes the mapping procedure that is used to determine the distribution of solid vs. liquid within the solid-liquid-wick mixture, as well as to determine the mixture temperature.

Section **Error! Reference source not found.** discusses changes made to the intercell fluxes associated with advection.

2.1 Constitutive Relations

Some liquid-solid-wick mixture quantities are defined as follows:

$$\alpha_{\ell sw} = \alpha_\ell + \alpha_s + \alpha_w, \tag{12}$$

$$(\alpha\rho)_{\ell sw} = \alpha_\ell \rho_\ell + \alpha_s \rho_s + \alpha_w \rho_w, \tag{13}$$

$$(\alpha\rho E)_{\ell sw} = (\alpha\rho)_{\ell sw} e_{\ell sw} + \frac{1}{2}\,\alpha_\ell \rho_\ell u_\ell^2, \tag{14}$$

$$e_{\ell sw} = Y_\ell e_\ell + Y_s e_s + Y_w e_w, \tag{15}$$

$$Y_i \equiv \frac{\alpha_i \rho_i}{(\alpha\rho)_{\ell sw}}. \tag{16}$$

The solid phase density is taken as constant, set to be the liquid density at the melting point because when the working fluid melts, it will appear with this density:

$$\rho_s = \rho_\ell(p_{\text{melt}}, T_{\text{melt}}). \tag{17}$$

Specific internal energies of the solid and wick use a simple linear heat capacity approximation:

$$e_s(T) = c_{v,s} T, \tag{18}$$

$$e_w(T) = c_{v,w} T. \tag{19}$$

Assuming the liquid, solid, and wick to be in thermal equilibrium, they share a common temperature of $T_{\ell sw}$. To determine the distribution of solid vs. liquid in the liquid-solid-wick mixture, a mixture specific internal energy is estimated by neglecting the kinetic energy of the liquid, which is a reasonable approximation, considering the very small liquid speeds encountered in a heat pipe:

$$\tilde{e}_{\ell sw} = \frac{(\alpha\rho E)_{\ell sw}}{(\alpha\rho)_{\ell sw}} \tag{20}$$

The value of α_ℓ is determined from this energy by linear interpolation between the energies e^* and e^{**}, which correspond to the pre- and post-melt end points of the melting process, respectively. Between these two values, the liquid volume fraction varies linearly from 0 to 1:

$$\alpha_\ell = \begin{cases} 0 & \tilde{e}_{\ell sw} \le e^* \\ (1-\alpha_v-\alpha_w)\frac{\tilde{e}_{\ell sw}-e^*}{e^{**}-e^*} & e^* < \tilde{e}_{\ell sw} < e^{**}, \\ 1-\alpha_v-\alpha_w & \tilde{e}_{\ell sw} \ge e^{**} \end{cases} \tag{21}$$

and then:

$$\alpha_s = 1 - \alpha_v - \alpha_w - \alpha_\ell. \tag{22}$$

An example of the volume fraction mapping is shown in Figure 1.

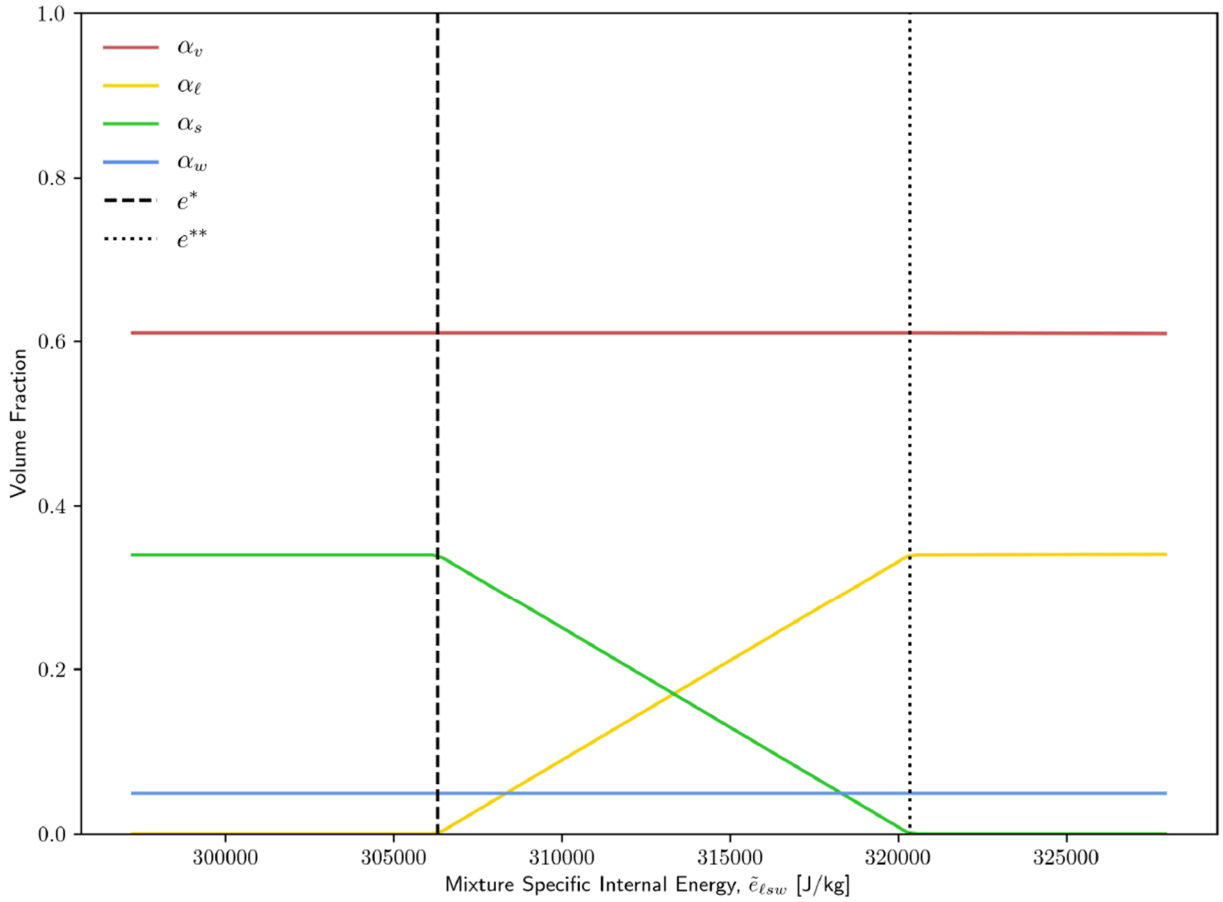

Figure 1. Example of the volume fraction mapping at the melting point.

The end points e^* and e^{**} are determined by evaluating $e_{\ell sw}$ at the melting temperature T_{melt} with $\alpha_\ell = 0$ and $\alpha_s = 0$, respectively:

$$e^* = \left((1 - Y_w)c_{v,s} + Y_w c_{v,w}\right) T_{\text{melt}}, \tag{23}$$

$$e^{**} = \left((1 - Y_w)c_{v,\ell} + Y_w c_{v,w}\right) T_{\text{melt}}, \tag{24}$$

$$Y_w = \frac{\alpha_w \rho_w}{\alpha_{\ell s}\rho_s + \alpha_w \rho_w}, \tag{25}$$

$$\alpha_{\ell s} = 1 - \alpha_v - \alpha_w. \tag{26}$$

For the liquid phase, a simple equation of state is used while the working fluid is a mixture of the liquid and solid phases, and a more sophisticated equation of state is used when only liquid is present, thus allowing equivalence to the two-phase model in the liquid-vapor regime:

$$e_\ell = \begin{cases} c_{v,\ell} T_{\ell sw} & \tilde{e}_{\ell sw} \le e^{**} \\ e_\ell(p_\ell, T_{\ell sw}) & \tilde{e}_{\ell sw} > e^{**} \end{cases}. \tag{27}$$

Here, the constant $c_{v,\ell}$ is computed such that the specific internal energy approximation is equal to the real equation of state specific internal energy at the point of melting; thus:

$$c_{v,\ell} = \frac{e_\ell(p_{\text{melt}}, T_{\text{melt}})}{T_{\text{melt}}}, \tag{28}$$

and the constant $c_{v,s}$ is computed to be consistent with the latent heat of fusion value Δh_{fus}, given by the equation of state:

$$c_{v,s} = c_{v,l} - \frac{\Delta h_{\text{fus}}}{T_{\text{melt}}}. \tag{29}$$

Now the mixture temperature is determined. If solid is present (i.e., $\tilde{e}_{\ell sw} \leq e^{**}$), then the mixture temperature can be determined as follows:

$$T_{\ell sw} = \begin{cases} \frac{e_{\ell sw}}{Y_s^* c_{v,s} + Y_w^* c_{v,w}} & \tilde{e}_{\ell sw} \leq e^* \\ T_{\text{melt}} & e^* < \tilde{e}_{\ell sw} \leq e^{**} \end{cases}, \tag{30}$$

and the liquid-specific internal energy is computed as:

$$e_\ell = c_{v,\ell} T_{\ell sw}. \tag{31}$$

For $\tilde{e}_{\ell sw} > e^{**}$, an approximate mixture temperature is determined for the purposes of estimating the energy stored in the wick:

$$\tilde{T}_{\ell sw} = \frac{e_{\ell sw}}{Y_\ell^{**} c_{v,\ell} + Y_w^{**} c_{v,w}}. \tag{32}$$

Then, the liquid-specific internal energy is computed as:

$$e_\ell = \frac{e_{\ell sw} - Y_w c_{v,w} \tilde{T}_{\ell sw}}{Y_\ell} \tag{33}$$

Finally, the actual mixture temperature is determined from the liquid equation of state:

$$T_{\ell sw} = T_\ell(v_\ell, e_\ell). \tag{34}$$

An example of the temperature mapping is shown in Figure 2.

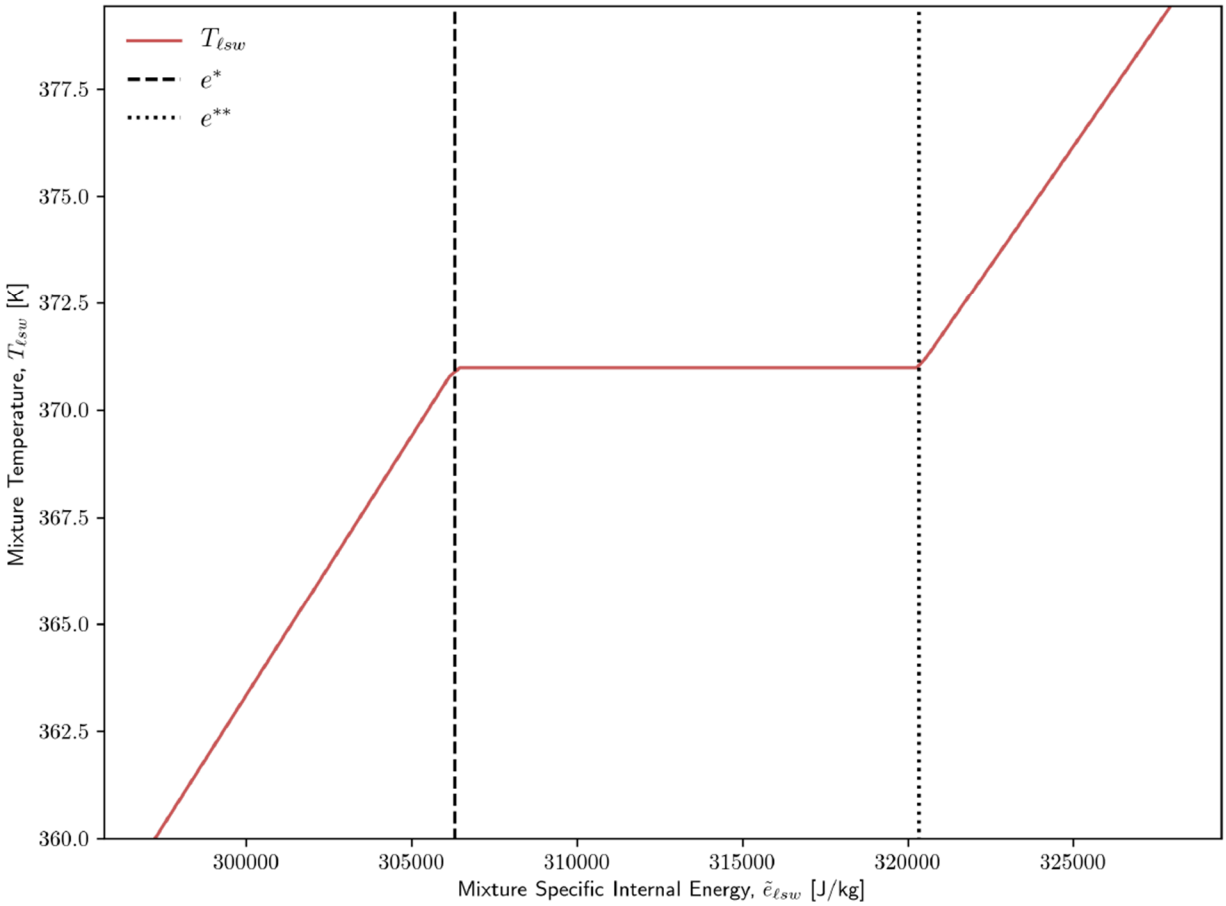

Figure 2. Example of the temperature mapping at the melting point.

2.2 Advection Changes During Melting

This section presents some preliminary changes made to advection when considering the presence of the solid phase. Note that these changes are not reflected in the results in Section 3 due to shortcomings in the equation of state—all advection (other than heat conduction) is disabled until the heat pipe is fully thawed. Therefore, these details are provided for future reference when improvements to the equation of state will allow for these capabilities to be demonstrated.

The finite volume discretization of the PDE system given in Section 2 is as follows:

$$|\Delta x_i| \frac{\mathrm{d}\mathbf{u}_{k,i}}{\mathrm{d}t} + \mathbf{f}_k(\mathbf{u}(x_{i+1/2})) - \mathbf{f}_k(\mathbf{u}(x_{i-1/2})) + \alpha_{k,i}(\mathbf{h}_k(\mathbf{u}(x_{i+1/2})) - (\mathbf{h}_k(\mathbf{u}(x_{i-1/2}))) \approx \int_{\Delta x_i} \mathrm{s}_k(\mathbf{u})\, \mathrm{d}x, \tag{35}$$

where k denotes the phase (v or ℓsw), i denotes the cell index, and the intercell fluxes are determined using an approximate Riemann solver:

$$\mathbf{f}_k(\mathbf{u}(x_{i+1/2})) \approx \mathcal{F}_{k,j}(\mathbf{U}_L, \mathbf{U}_R, A_L, A_R, n_{L,R}). \tag{36}$$

The existing two-phase approximate Riemann solver is modified as follows for the three-phase model. A number of cases are now considered for the combination of left and right solutions, $\mathbf{U}_L$ and $\mathbf{U}_R$, respectively:

- **Neither *L* nor *R* have a solid phase.** The flux is computed exactly as it was for the two-phase model.
- **Both *L* and *R* have a solid phase, but no liquid phase.** The flux is computed exactly as it was for the two-phase model.
- **One of either *L* or *R* has a solid phase, but no liquid phase.** Wall conditions are applied to the side with liquid, while zero flux is used on the other. Wall conditions are applied by computing the flux with a ghost solution, $\mathbf{U}_{\text{wall}}$ that is the same as $\mathbf{U}$ but with reversed velocities, which creates a reflective flux. Note that these flux modifications are applied to both phases, not just the ℓsw phase, to be consistent with the observation that the vapor continuum front roughly follows the melt front. Alternatively, the vapor phase could be allowed to traverse the entire heat pipe. Both of these approaches are approximations; validation efforts will guide the selection of the most accurate approach.
- **One or both of *L* or *R* have a mixture of the liquid and solid phases.** In this case, the liquid and vapor phases are treated as separate, single-phase, variable-area channels.

3. NUMERICAL DEMONSTRATIONS

3.1 Startup

This test problem features a sodium heat pipe using parameters given in Table 1, which begins at 300 K (approximately room temperature) and then transitions into a full, two-phase operation over the course of 3500 seconds.

Table 1. Heat pipe parameters for startup test problem.

Parameter	Value
Length of evaporator region	0.3 m
Length of adiabatic region	0.4 m
Length of condenser region	0.3 m
Inner diameter of wick	1.74 cm
Outer diameter of wick	2.07 cm
Inner diameter of cladding	2.21 cm
Radius of a wick pore	30 μm
Porosity of wick	0.8073
Permeability of wick	10^{-10} m^2
Wick density	7900 kg/m^3
Wick specific heat capacity	500 J/(kg-K)
Wick thermal conductivity	15 W/(m-K)
Working fluid	Sodium
Wick fill ratio	1.05 at 800 K
Solid thermal conductivity	140 W/(m-K)

Convective heat transfer conditions are applied along the entire heat pipe length:

$$q_{\ell sw}^{\text{wall}} = \mathcal{H}(T_{\text{env}} - T_{\ell \text{sw}}), \tag{37}$$

with the heat transfer coefficient $\mathcal{H}$ and the environment temperature T_{env} varying over the course of the transient and by axial section:

$$\mathcal{H}_{\text{evap}}(t) = \mathcal{H}_{\text{cond}}(t) = \begin{cases} 10 & t \le 1000 \\ 10 + (100 - 10)(t - 1000)/1000 & 1000 < t \le 2000 \\ 100 & t > 2000 \end{cases}, \tag{38}$$

$$\mathcal{H}_{\text{adia}}(t) = \begin{cases} 10 & t \le 1000 \\ 0 & t > 1000 \end{cases}, \tag{39}$$

$$T_{\text{env,evap}}(t) = \begin{cases} 700 & t \le 1000 \\ 700 + (900 - 700)(t - 1000)/1000 & 1000 < t \le 2000 \\ 900 & t > 2000 \end{cases}, \tag{40}$$

$$T_{\text{env,adia}} = T_{\text{env,cond}} = 700. \tag{41}$$

While designing this test problem, it was discovered that uniform heating during the melting process was necessary to avoid calls into states not recognized by the limited sodium equation of state. Due to an advancing melt front, pressure spikes occur due to advancing wall boundary conditions, and the corresponding (v, e) function produces an invalid state. This reveals a need to expand the range of validity of the equation of state before general startup transients can be run robustly.

Error! Reference source not found. shows the temperature transient, including the environmental temperatures driving the transient, while Figure 4 shows the power transients in the evaporator and condenser regions. Initially, the heat-up is uniform; all of the heat pipe is exposed to an environment temperature of 700 K until 1000 s, when the evaporator environmental temperature starts to increase to its final value of 900 K at 2000 s, at which the condenser heat transfer direction finally reverses due to heat pipe temperature exceeding the condenser environment temperature. Because both the evaporator and condenser are the same length and have the same heat transfer coefficient, the steady-state operating temperature is approximately the average of the two environment temperatures. One can see that the minimum temperature of the heat pipe dips a small amount at the end of the transient, which is due to the formation of a small condenser pool. Note the overshoot in Figure 4 is physical, due to the increasing temperature of the heat pipe, paired with the end of the heat transfer coefficient and wall temperature ramps.

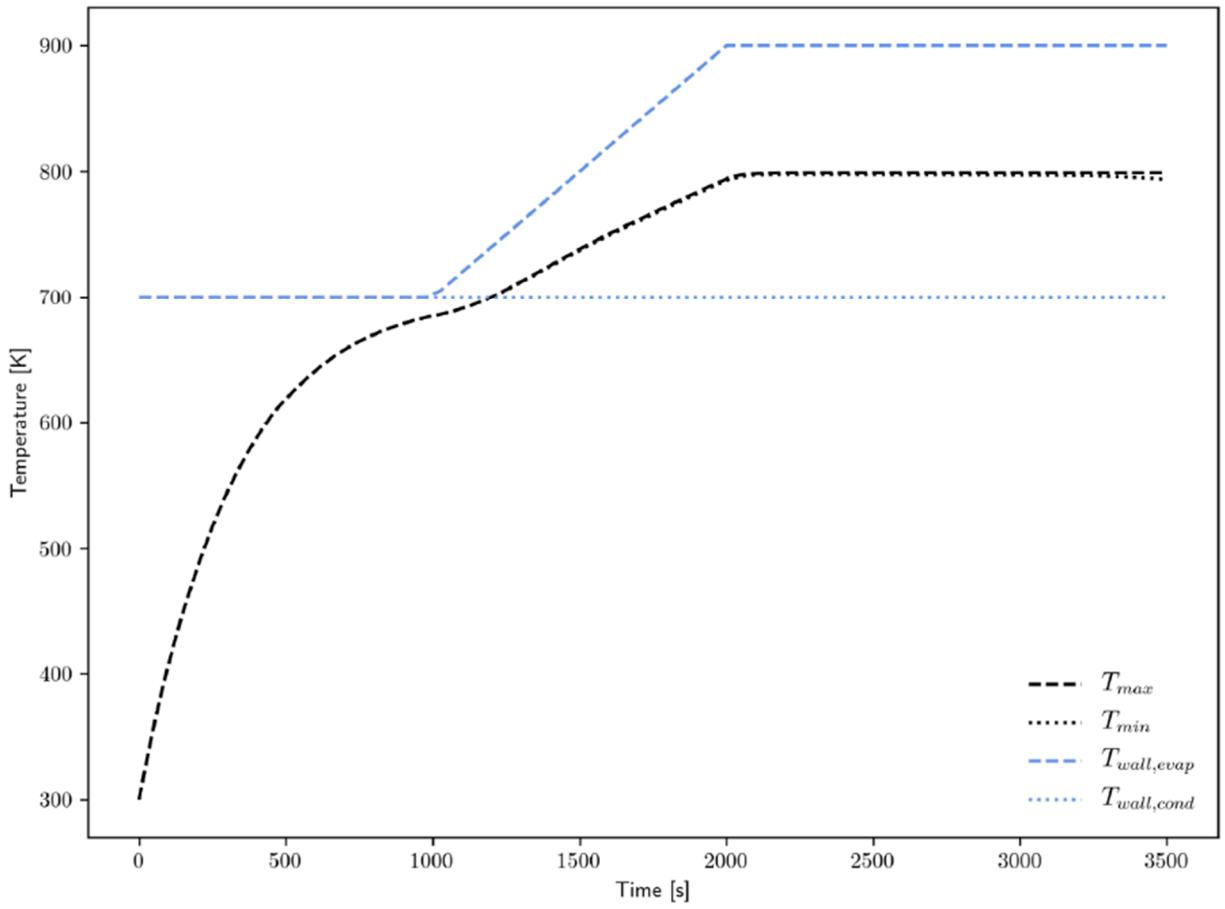

Figure 3. Temperature transient for startup test problem.

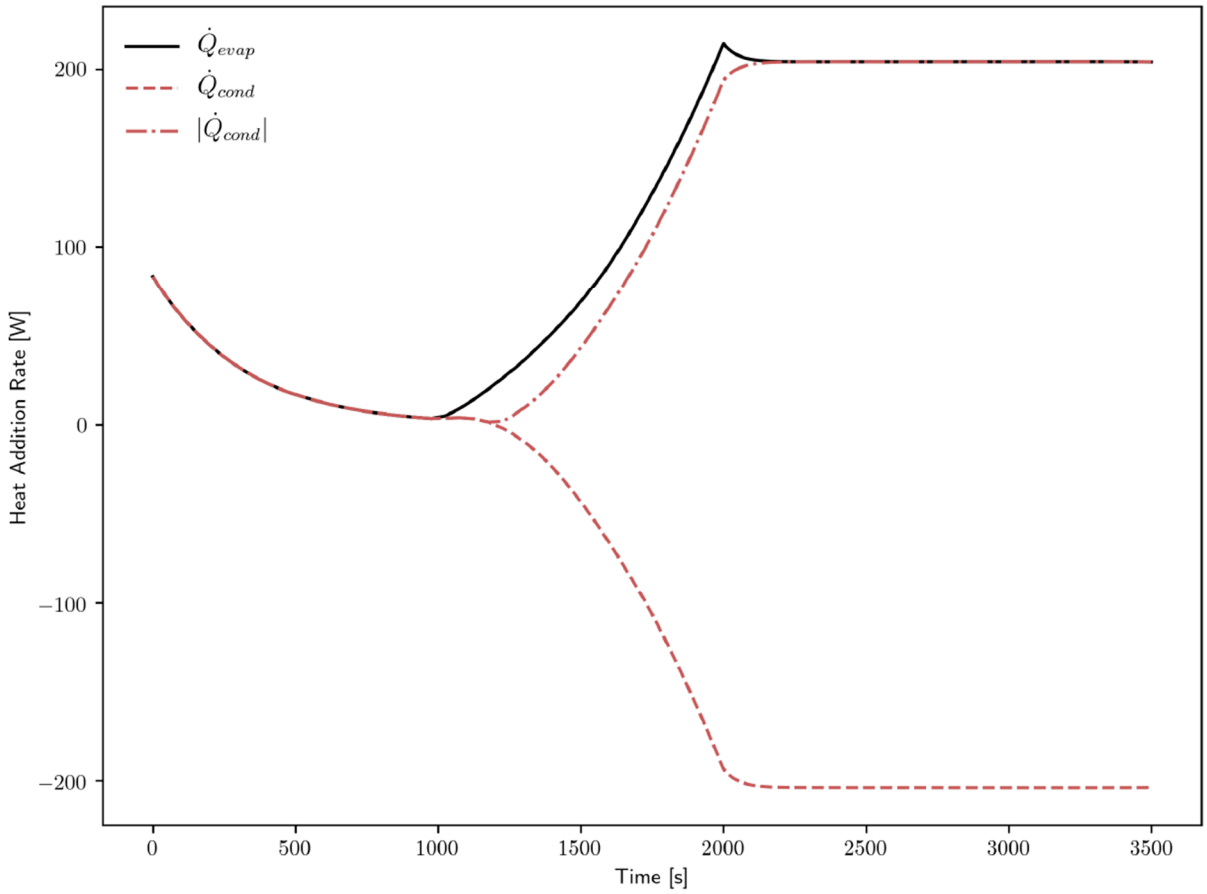

Figure 4. Evaporator and condenser heat rate transient for startup test problem.

Figure 5 shows the final temperature distribution, indicating a nearly isothermal operation, except for the condenser pool, which can be seen in Figure 6. The liquid-vapor interface recedes into the wick slightly, giving rise to a positive capillary pressure, which can be seen in Figure 7. The small permeability of the wick gives rise to a large pressure drop in the liquid phase, going from the condenser to the evaporator. The comparatively small pressure drops due to acceleration and recovery in the vapor phase are also evident. Figure 8 shows the final velocity profiles; the vapor phase shows its theoretical behavior due to mass injection and extraction, and the liquid phase possesses the same behavior, but in the opposite direction at a much smaller magnitude due to the significant density discrepancy.

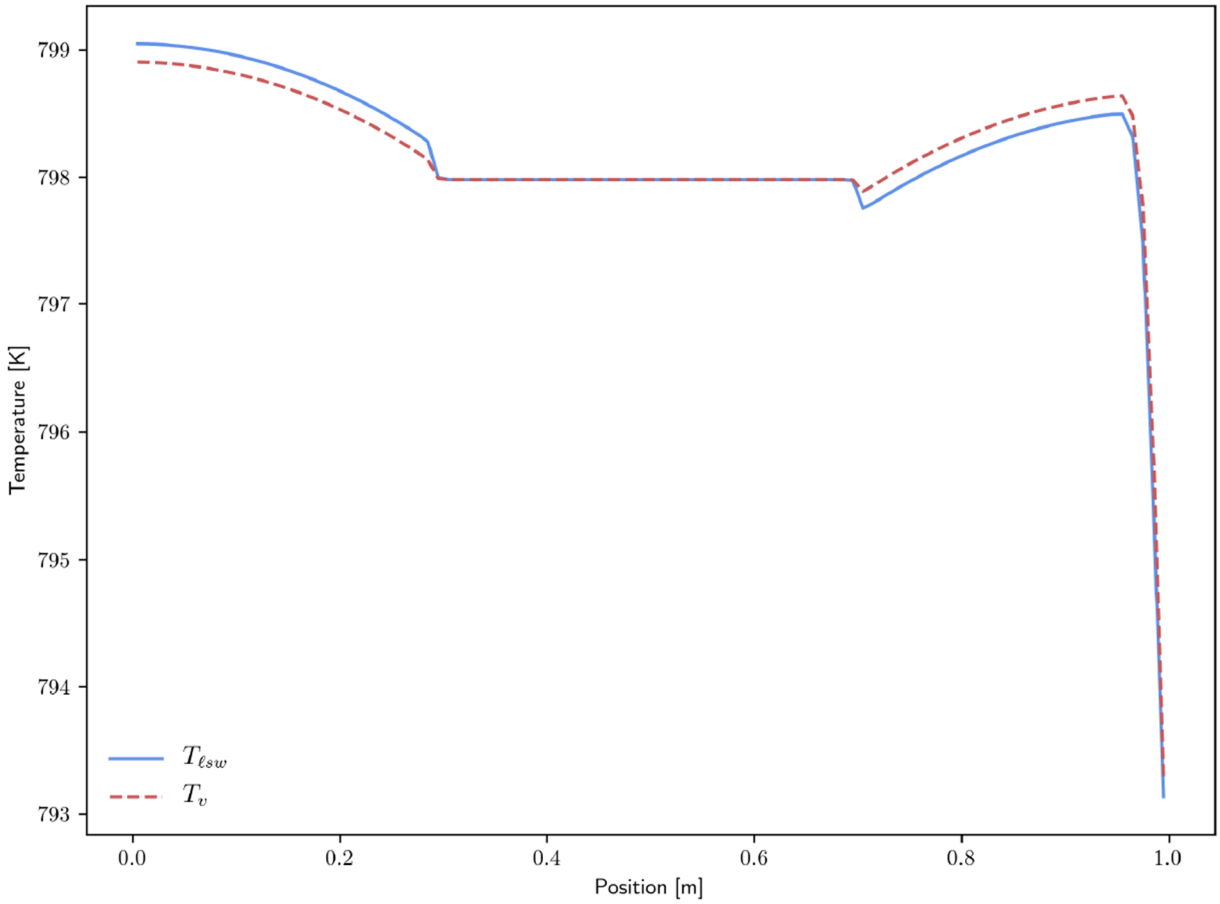

Figure 5. Temperature profiles for startup test problem.

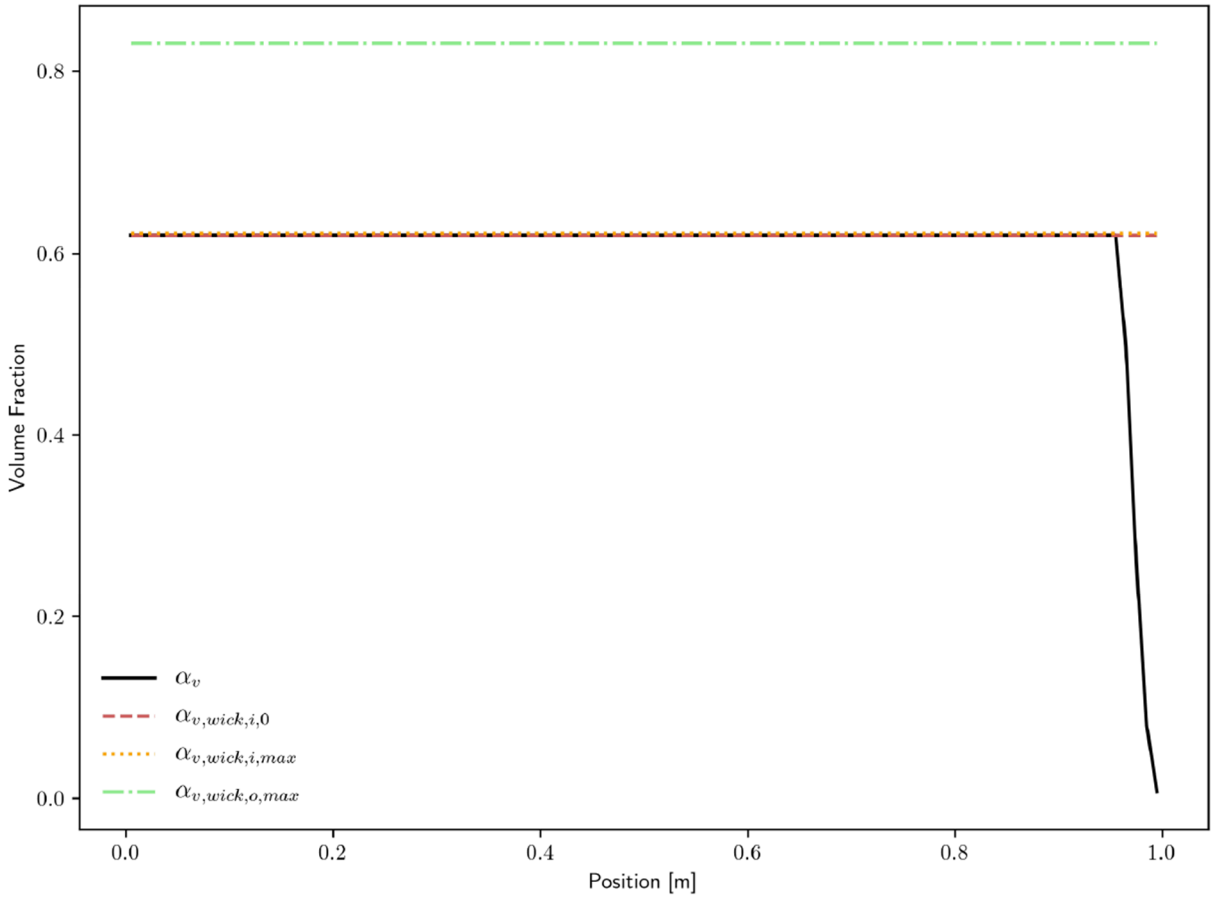

Figure 6. Void fraction profile for startup test problem.

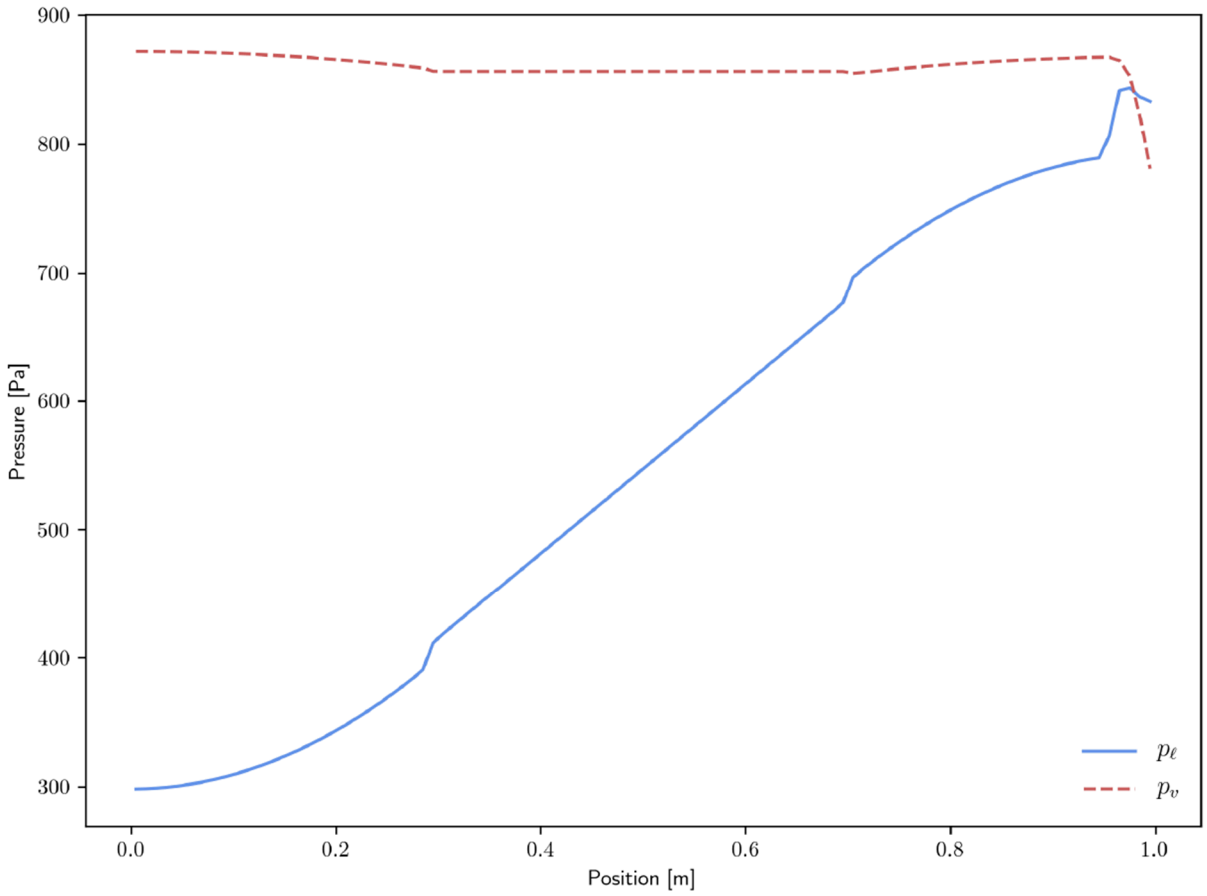

Figure 7. Pressure profiles for startup test problem.

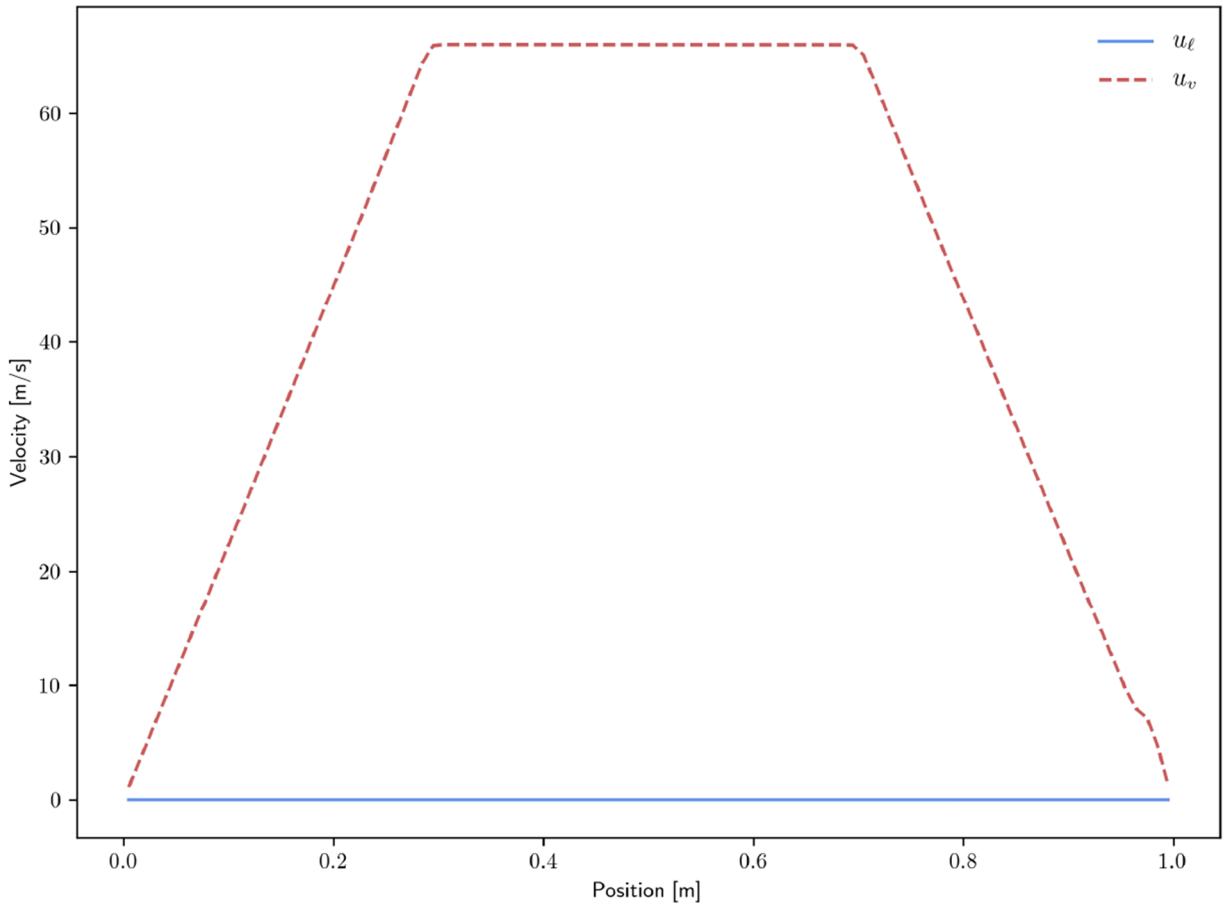

Figure 8. Velocity profiles for startup test problem.

3.2 Melt Front Propagation

This test problem features the same heat pipe design as used in Section 3.1, but the transient consists of a slow, non-uniform startup that demonstrates the propagation of the melt front. The initial temperature in the heat pipe is 360 K, and a power of 1 W is applied to the evaporator section over a time interval of 5000 seconds.

Figure 9 and Figure 10 show the temperature and liquid volume fraction profiles at different points in the transient. Note that the three-phase model sets the vapor phase to be at the melting temperature because it does not have an equilibrium state below the triple point. Since the initial temperature of 360 K is below the melting point temperature of 371 K for sodium, there is initially no liquid phase (i.e., $\alpha_\ell = 0$). As the transient progresses, the solid sodium melts, starting from the evaporator end and propagating toward the condenser end. With advection disabled during the melt, axial thermal conduction is the only effect that propagates the melt front, which occurs very slowly. The no-advection approximation is reasonable for the liquid phase, which has a very small speed; however, the lack of advection in the vapor phase is not physical, but simply a temporary necessity for model robustness, given the need to improve the equation of state in this regime. Realistically, the vapor starts in the free molecular regime and gradually develops a front of continuum vapor that propagates during the transient [1]. The advection of the vapor helps speed up the startup process by moving thermal energy down the length of the heat pipe, faster than thermal conduction in the liquid/solid alone.

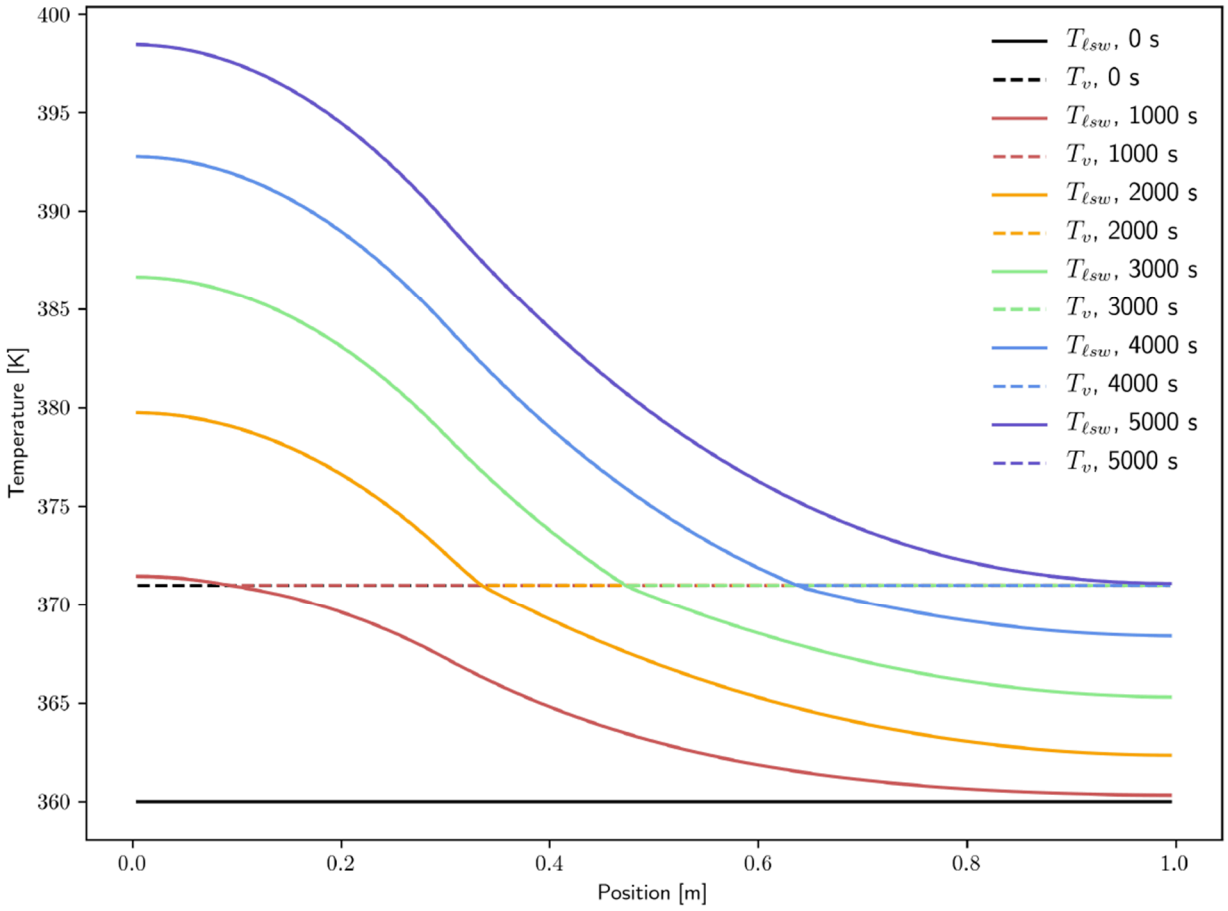

Figure 9. Velocity profiles for startup test problem.

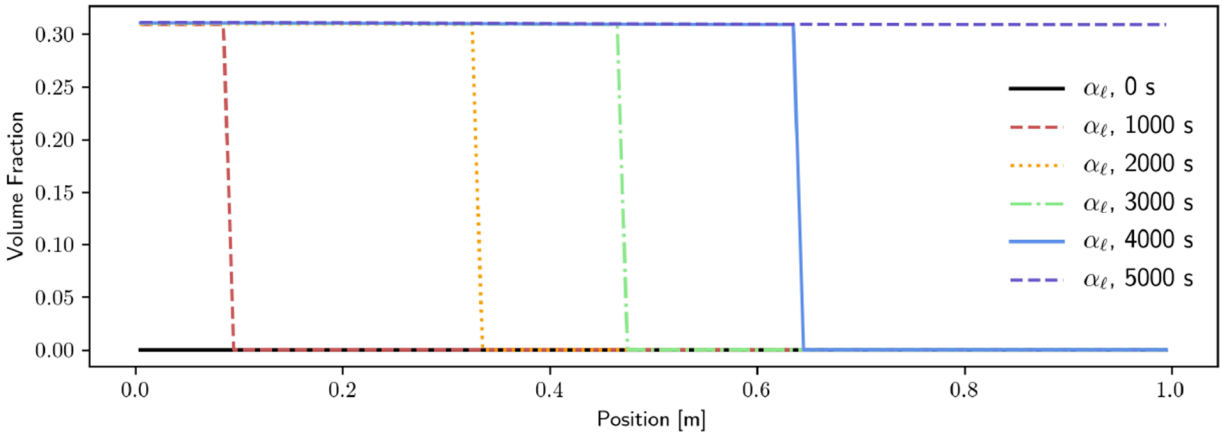

Figure 10. Liquid volume fraction profiles at different times during the melt front test problem.

4. CONCLUSIONS

Two demonstrations featured startup from temperatures at which the working fluid was fully frozen. The first featured a uniform heating to start up the heat pipe and went to its normal operating condition. The second showed a non-uniform heating, which lead to a melt front that propagated to the other end of the heat pipe. However, additional work on equations of state was found to be necessary for robust simulation in the startup/shutdown regimes.

When the saturation curve is followed carefully, the sodium equation of state returns valid states; however, startup features small pressure transients that result in leaving the range of validity in the equation of state. This could be either because the physics governing these transients is inaccurate, and thus that the state should not have been reached at all, or it could be that the physics are acceptable and the thermodynamic state is actually valid, in which case the equation of state is to blame. Regardless of whether the first reason is partly to blame, it is imperative that the equation of state be forgiving to allow simulations to continue, even if in these regimes, the equation of state is not perfectly accurate.

Another need that was highlighted by the numerical experiments was the need for robust phase disappearance. Phase disappearance of the liquid phase below the melting point or the solid phase above the melting point was found to work perfectly robustly, but the disappearance of either the vapor phase or the liquid phase when the working fluid is thawed are issues that remain from the two-phase model. Both of these scenarios are regularly encountered: vapor disappearance occurs with the formation of a liquid condenser pool, which is very common during normal operation, and liquid disappearance occurs during dryout, which is an accident condition but should be able to be modeled nonetheless. After phase disappearance is addressed, initial conditions may be extended to allow the working fluid to be frozen in a generic distribution, such as all pooled on one end of the heat pipe, rather than uniformly distributed throughout the heat pipe.

After the robustness of the equations of state in the startup regime are addressed, validation efforts should be conducted to assess the accuracy of the flow model used for startup. For example, it may be revealed that special treatment of the free molecular regime may be necessary.

5. REFERENCES

[1] Faghri, A. (2016) Heat Pipe Science and Technology, second edition. Global Digital Press, Columbia, MO, USA.

[2] Hall, M.J., and Doster, J.M. (1990) "A sensitivity study of the effects of evaporation/condensation accomodation coefficients on transient heat pipe modeling," *Int. J. Heat Mass Trans.*, 33(3): 465–481.

[3] Tournier, J.-M., and El-Genk, M.S. (1994) "A heat pipe transient analysis model," *Int. J. Heat Mass Trans.*, 37(4):753–762.

[4] Cao, Y., and Faghri, A. (1993) "A numerical analysis of high-temperature heat pipe startup from the frozen state," *J. Heat Trans.*, 115(1):247–254.

[5] Hansel, J.E., Berry, R.A., Andrš, D., and Martineau, R.C. (2019) Sockeye Theory Manual, Technical Report INL/EXT-19-54395, June 2019, Idaho National Laboratory, Idaho Falls, ID, USA.

[6] Hansel, J.E., Andrš, D., Berry, R.A., and Martineau, R.C. (2019) Sockeye: A 1-D Heat Pipe Modeling Tool, Technical Report INL/EXT-19-55742, September 2019, Idaho National Laboratory, Idaho Falls, ID, USA.

[7] Berry, R.A., Hansel, J.E., Kunick, M.S., and Martineau, R.C. (2020) Sockeye heat pipe code theory development: Based on the seven-equation, two-phase flow model of RELAP-7. In: *International Topical Meeting on Advances in Thermal Hydraulics (ATH'20), EDF Lab Paris-Saclay, France*. American Nuclear Society, La Grange Park, IL, USA.